First-principles melting of krypton and xenon based on many-body relativistic coupled-cluster interaction potentials

O. R. Smits,[1,*] P. Jerabek,[2,†] E. Pahl,[3,1,‡] and P. Schwerdtfeger[1,§]

[1]*Centre for Theoretical Chemistry and Physics, The New Zealand Institute for Advanced Study, Massey University Auckland, Private Bag 102904, 0632 Auckland, New Zealand*

[2]*Nanotechnology Department, Helmholtz-Zentrum Geesthacht, Max-Planck-Straße 1, 21502 Geesthacht, Germany*

[3]*The MacDiarmid Institute for Advanced Materials and Nanotechnology, Department of Physics, University of Auckland, New Zealand*

(Received 2 December 2019; revised manuscript received 24 February 2020; accepted 4 March 2020; published 24 March 2020)

The solid-to-liquid phase transition for krypton and xenon is studied by means of parallel-tempering Monte Carlo simulations based on an accurate description of the atomic interactions within a many-body ansatz using relativistic coupled-cluster theory. These high-level data were subsequently fitted to computationally efficient extended Lennard-Jones and extended Axilrod-Teller-Muto types of interaction potentials. Solid-state calculations demonstrate that the many-body decomposition of the interaction energy converges well for the heavier rare gas solids, leading to solid-state properties in good agreement with experiment. The results show that it suffices to include two- and three-body interactions only for the melting simulation. The melting of the bulk is simulated for cells with cubic periodic boundary conditions, as well as within a finite cluster approach. For the latter, melting of spherical magic number clusters with increasing cluster size is studied, and the melting temperatures are obtained from extrapolation to the bulk. The calculated melting temperatures for the cluster extrapolation (the periodic approach values corrected for superheating are set in parentheses) are $T_m = 113.7$ K (110.9 K) and $T_m = 160.8$ K (156.1 K) for krypton and xenon, respectively. Both are in very good agreement with corresponding experimental values of 115.75 and 161.40 K.

DOI: 10.1103/PhysRevB.101.104103

I. INTRODUCTION

Melting is a fundamental process in which a crystal undergoes a phase transition from a solid (ordered) state to a liquid (disordered) state. Fundamentally understanding the processes of melting at the microscopic level has proven to be rather difficult [1], and many theories have been developed during the past century resulting in a range of different frameworks that tackle the problem of melting from different perspectives. For example, as proposed by Lindemann [2], the first-order phase transition occurs at the temperature at which the amplitude of atomic thermal vibrations reaches a characteristic value. At this point melting is triggered by a mechanical instability, causing the atoms to move from their ordered state to a disordered fluid. By using this principle, it is possible to determine the melting point by observing the average motion of the atoms in a system. For instance, the Etters-Kaelberer parameter [3,4] and the Berry parameter [5] are proportional to the fluctuations of the interatomic distances. These parameters suddenly increase at the melting point and may therefore be used as the definition of the melting temperature.

Although different criteria that define the melting transition (and quantities that distinguish the solid and the liquid states) can be formulated, it is clear that the underlying cause of melting is the minimization of Helmholtz free energy F (or Gibbs energy G), which is an interplay between minimizing the inner energy U (enthalpy H) and maximizing the entropy S at constant volume (pressure). Other quantities such as the disappearance of shear moduli [6] or increase of fluctuations of interatomic distance are resulting quantities.

With regards to the minimization of the free energy, that is, at $T < T_m$, the free energy of the solid is smaller than the free energy of the liquid and vice versa at $T > T_m$, whereas at the melting temperature the solid and the liquid are in thermodynamic equilibrium. Thus, at the phase transition, $F_s(V, T_m) = F_l(V, T_m)$ or $G_s(p, T_m) = G_l(p, T_m)$ for constant volume or pressure, respectively. The free energies are a function of volume (pressure) and temperature during the first-order phase transition, but other quantities, like the internal energy U or enthalpy H, the entropy S, volume V or pressure P, and heat capacities C, undergo discontinuous changes. For example, upon melting, the inner energy suddenly increases and the heat capacity C_v (C_p) at constant volume (pressure) will become infinite. For finite clusters and in numerical simulations, the singularity in the heat capacity shows as a peak at the phase transition, which allows one to easily identify the melting point.

When it comes to simulating melting numerically, two approaches are popular. Molecular dynamics (MD) is a

*smits.odile.rosette@gmail.com
†paul.jerabek@gmail.com
‡elke.pahl@auckland.ac.nz
§peter.schwerdtfeger@gmail.com; http://ctcp.massey.ac.nz/

time-dependent simulation, in which the positions of the atoms are determined by solving Newton's second law or the equation of motion for a range of different temperatures, whereas Monte Carlo (MC) approaches are based on random sampling. Opposed to gaining insight on the time evolution of a system, an ensemble of statistically representative configurations is obtained and, consequently, the relevant thermodynamic observables, such as the free energy or heat capacity, may be calculated. Both methods have their advantages and disadvantages. The so-called parallel tempering MC (PTMC) method [7] explores phase space very efficiently by simultaneously sampling at different temperatures allowing for information exchange between different trajectories. As such, this method gives more easily access to the transition temperature than in MD simulations. In both approaches, the dynamics of the system studied is described classically, which is adequate for all but the lightest atomic systems like helium. For neon, it was shown that quantum effects can be detected but are still negligible [8]. The heavier bulk rare gases investigated in this study can thus be described by a classical treatment of the dynamics.

In contrast to the classical description of the dynamics, it is important to use a highly accurate quantum-mechanical description of the interaction energies. A many-body expansion of the total interaction energy provides a successful approach for weakly interacting systems. By summing up all two- and, if necessary, three-body contributions, the total interaction is described reasonably well. Data for the required two- and three-body interaction potentials are obtained through high-level quantum-mechanical computations which are subsequently fitted to computationally efficient functions. For example, for the heavy rare gases, the two- and three-body interaction potentials can be obtained via an extended Lennard-Jones [9] fit to relativistic coupled-cluster data performed prior to the simulation.

The most common method to study melting is by performing simulations of a perfect lattice with periodic boundary conditions for increasing temperatures. The temperature at which the lattice breaks down corresponds to the melting temperature. The problem with such a method is that due to the absence of a surface the system melts at a much higher temperature as observed experimentally, referred to as superheating. Similarly, when a liquid is cooled down the phase-change temperature is underestimated due to the existence of supercooling. This behavior is a hysteresis phenomenon. Supercooling and superheating are not just problems in theoretical simulations, but are observed experimentally as well and are currently a matter of intense research [10].

One can determine an approximation to the melting point T_m from the hysteresis method via $T_m = T^+ + T^- - \sqrt{T^+T^-}$ with T^+ and T^- being the temperatures observed for superheating and supercooling [11,12]. In order to eliminate superheating in simulations, defects can be introduced into the bulk system as they are found to lower the observed melting point [13,14]. That is done by either displacing atoms from their equilibrium solid-state position or alternatively by removing atoms from the simulation cell. The impurities and vacancies introduced in the supercell create nucleation sites and eliminate the free energy barrier such that the solid melts at the "true" melting temperature rather then the superheated temperature. The void method is based on this principle using supercells with vacancies introduced in the solid structure [15]. The computed melting point decreases with the increasing concentration of voids until the melting point is independent of the number of voids; however, this method requires large numbers of atoms, N, in the unit cell for the simulation. For computational affordability, we chose to perform simulations of periodic cells without impurities or defects and instead correct the superheated temperature of the solid-to-liquid phase transition by a superheating factor. To circumvent hysteresis we also simulated the melting of krypton and xenon by studying the melting of finite clusters. Since cluster melting is initiated at the surface of the cluster, superheating does not occur (instead one might observe premelting at the surface). The melting temperature of the bulk can then be obtained from extrapolation of the melting points of the smaller clusters to the bulk.

Experimentally, the triple points of krypton and xenon were determined in the early 20th century. The first to publish an accurate value for krypton were Allen and Moore [16] in 1931, who reported a triple point of 116.7 ± 0.1 K. They stated that the triple point was best observed by getting solid krypton in an apparatus "as much as a fluffy and snow-like form as a possible" and found the melting point from observation as the temperature rose. Multiple similar values were later obtained: for example, Keesom *et al.* [17] reported a triple point of 115.94 K in 1935 and Freeman and Halsey [18] reported a value of 115.6 K. Recently the triple point was confirmed by Hill [19] up to high accuracy, who obtained a triple point of 115.7755 ± 0.3 mK. The triple-point value of 133.15 K for xenon was first obtained by Ramsay and Travers [20] in 1901, after which Allen and Moore [16] obtained the improved value of 157.65 ± 0.5 K. A melting point of 161.3 K was reported by Kane [21] in 1939 and after that an improved value was determined to be 161.40 K [22]. A more recent evaluation of these data can be found in the work by Ferreira and Lobo [23].

In our previous work we demonstrated that melting temperatures for the lighter rare gases neon and argon can be obtained within Kelvin accuracy from first-principles theory [8]. In fact, for solid argon a rigorous expansion of the interaction energy in terms of many-body potentials derived from coupled-cluster theory including phonon dispersion led to an unprecedented μHa accuracy for the cohesive energy [24]. Such high accuracy in the atomic interactions is crucial for the simulation of phase transitions [14]; e.g., it is well known that there is a strong correlation between the cohesive energies and melting temperatures of a bulk system [25,26]. High-level simulations based on *ab initio* data led recently to the confirmation of the much-debated melting temperature of radon [27,28], and to corrections of measured melting temperatures of argon at high pressures [29].

In this work we study the solid-to-liquid phase transition for the heavier rare gas systems krypton and xenon by applying a many-body interaction potential derived from rigorous relativistic electronic structure theory in conjunction with PTMC simulations. These bulk systems are interesting as the higher n-body contributions in the decomposition of the

interaction energy become more important with increasing dipole polarizability for the heavier rare gas atoms [30,31]. We present *ab initio* many-body potentials derived from relativistic coupled-cluster theory and apply them to the solid to obtain bulk properties. Then, the melting temperatures of the clusters and the extrapolation to the bulk melting temperature are presented from parallel tempering MC simulations and compared with the results obtained from experimental work.

II. COMPUTATIONAL DETAILS

The interaction potential. The many-body interaction potential $E_{\rm int}(N)$ for an N atomic system can be expanded into sums over all possible two-body $E^{(2)}$, three-body $E^{(3)}$, and higher-order $E^{(n)}$ contributions,

$$E_{\rm int}(N) = \sum_{n=2}^{N} E^{(n)}(N) = \sum_{i<j}^{N} E^{(2)}(r_{ij}) + \sum_{i<j<k}^{N} E^{(3)}(r_{ij}, r_{ik}, r_{jk}) + \cdots , \quad (1)$$

where r_{ij} is the distance between atoms i and j. The many-body expansion converges rapidly at normal pressures and temperatures for the rare gas elements, or more generally for weakly interacting atoms and molecules [32,33] (it is, however, well known to converge badly for most other systems such as metals [34]). For instance, for bulk argon the two-body interaction overshoots the exact binding energy by only 8% with each higher n-body contribution diminishing by an order of magnitude with increasing n [24]. One can therefore expect that bulk properties of krypton and xenon at ambient conditions are satisfactorily described by considering two- and three-body terms only. In order to put this assumption to the test, we used dimer and trimer potentials from a relativistic coupled-cluster expansion and fitted the data to computationally efficient functional forms for our MC simulation.

For krypton we adopted the already available *ab initio* two-body potential calculated by Jäger *et al.* [35]. The authors obtained the interaction energies at the complete basis set limit using the coupled-cluster method with single, double, and perturbative triple excitations for 36 interatomic distances between 2.2 and 15 Å. Higher orders of coupled-cluster terms were also considered in a successive scheme up to full quadruple excitations. Core-core and core-valence correlation effects were included. Furthermore, relativistic effects were also studied not only at a scalar relativistic level using second-order direct perturbation theory, but also utilizing a full four-component computation including Gaunt interactions [35]. For xenon an accurate potential energy curve has been derived by our group using coupled-cluster theory up to quadruple excitations accounting for both basis set superposition and incompleteness errors and has been extrapolated to the complete basis set limit. Scalar relativistic effects were considered via a second-order Douglas-Kroll-Hess (DKH2) approximation, and the X2C-Gaunt approximation was employed to obtain the spin-orbit correction. To construct the xenon pair potential the dimer interaction energy was determined over 30 distances selected in the range from 2.5 to 16.0 Å. Details can be found in Ref. [30].

TABLE I. Potential parameters for the krypton and xenon two- and three-body interactions obtained from a fit of *ab initio* data to an ELJ and EATM potential, respectively [30]. All potential parameters are given in atomic units.

ELJ	Krypton	Xenon
c_6	–129.683335093935	–301.700000000000
c_8	–158598.441365431	–26816.4020712100
c_9	15623507.6830131	–29141425.4118978
c_{10}	–662519888.486613	2525729440.60837
c_{11}	15511005394.0185	–93157553751.1815
c_{12}	–221232142140.590	1958061699137.66
c_{13}	1994087272787.29	–25959609531187.9
c_{14}	–11387455618340.6	225015902487099
c_{15}	39946814675145.8	–1272921381781360
c_{16}	–78619450156252.0	4526862108942420
c_{17}	66546834460178.8	–9182845674164360
c_{18}		8100817151233590
EATM	**Krypton**	**Xenon**
$C_{\rm EAT}$	1606.77610926838	3471.93012715399
A_0	60036.9547561167	886.992268260218
A_2	–3670.25288702589	–132.687520259295
A_4	25.6338653669989	3.14321647514269
A_6	0.30585091087561	–0.01977876625979
α	0.98918853451850	0.68379059500687

The data points for those potential curves were pointwise fitted to an extended Lennard-Jones (ELJ) potential [9] by a linear least-squares procedure

$$E^{(2)}_{\rm ELJ}(r_{ij}) = \sum_{k=0}^{n} c_{k+6} r_{ij}^{-(k+6)}, \quad (2)$$

where r_{ij} is the internuclear distance between atoms i and j and c_k are the fitting parameters. To ensure that the long range is described solely by the attractive $c_6 r^{-6}$ part of the potential, the c_7 coefficient is excluded from the ELJ potential. Furthermore, to ensure correct repulsive asymptotic behavior in the short range, the highest-order fitting parameter must be positive. The advantage of this simple potential is that it is nearly as accurate as the extended Aziz potential in both the short and the long range, while it performs computationally as efficiently as the Lennard-Jones potential [36]. Fitting coefficients are listed in Table I. The root-mean-square errors (RMSEs) for the fit were 1.29×10^{-7} and 9.32×10^{-7} Ha for Kr_2 and Xe_2, respectively.

The nonadditive three-body interaction energies for krypton were calculated for 14 trimer geometries as equilateral triangles with bond lengths between 3.0 and 7.5 Å. The MOLPRO 2015.1 program package [37] was used to compute electronic energies at the CCSD(T)-DKH2$_{(4s4p)}$/aug-cc-pwCVQZ-DK2 level of theory. The corrections from correlating subvalence electrons were estimated from the difference between all-electron MP2-DKH2/aug-cc-pwCVQZ-DK2 and MP2-DKH3$_{(4s4p)}$/aug-pwCVQZ-DK2 calculations.

The three-body correction becomes more important for the heavier rare gas xenon. Here the nonadditive interaction

energy for 300 different xenon trimer configurations (with Xe-Xe distances between 2.1 and 7.9 Å) was computed at the CCSD(T)$_{(5s5p)}$/aug-pwCVQZ-DK level of theory. The correlation of subvalence electrons was estimated with second-order Møller-Plesset perturbation theory (MP2) as [MP2 (AE)-MP2$_{(5s5p)}$]/QZ. Following the same method as proposed by Cencek *et al.* [38], the 300 trimer geometries were then chosen to represent the most important points on the potential energy surface. For both krypton and xenon potentials counterpoise correction was applied to account for the basis set superposition error.

These three-body corrections $E^{(3)}(r_{ijk})$ were fitted to a computer-efficient extended Axilrod-Teller-Muto (EATM) potential [39]:

$$\begin{aligned} E^{(3)}_{\mathrm{EATM}}(r_{ijk}) &= f_\theta\left[C_{\mathrm{EAT}}R_g^{-9} + (A_0 + A_2R_g^2 + A_4R_g^4 + A_6R_g^6)e^{-\alpha R_s}\right] \\ &\text{with } f_\theta = (1 + 3\cos\theta_i\cos\theta_j\cos\theta_k), \\ &\quad R_g = (r_{ij}r_{jk}r_{ik})^{1/3}, \\ &\text{and } R_s = r_{ij} + r_{jk} + r_{ik}, \end{aligned} \tag{3}$$

where r_{ij} is the distance between atoms i and j, and θ_i is the angle between the vectors $\vec{r}_{ij}$ and $\vec{r}_{ik}$. The fitting parameters of krypton were obtained by a least-squares fit over the 14 equilateral distances. For xenon, the C_{EAT} parameter was first obtained from a least-squares fit over the long-range equilateral *ab initio* data points. Subsequently, the value of C_{EAT} was kept fixed and all other parameters were obtained by a least-squares fit to the 300 *ab initio* energies including also the nonequilateral region of space. The parameters C_{EAT}, A_n, and α are also listed in Table I. The RMSE of the EATM fit for the krypton is 3.06×10^{-7} and that for xenon is 5.13×10^{-3}. The *ab initio* data points are equilateral only for krypton but also nonequilateral for xenon. The RMSE for krypton is therefore smaller than the RMSE of xenon, whereas in fact the xenon potential describes the potential energy surface more accurately.

Solid-state calculations. The interaction potentials were used to calculate the lattice constants, cohesive energies, and bulk moduli for the face-centered cubic (fcc) arrangement of the bulk to compare with available experimental values. While the ELJ two-body contribution including vibrational corrections for the fcc solid was treated analytically through lattice sums [9], the three- and four-body additive corrections came from numerical lattice summations using the program system SAMBA [24]. The three-body forces are of extended Axilrod-Teller-Muto type from this work, and four-body forces were obtained from the fourth-order classical dipole term as described in detail by Bade [40] and by our group [24]. The corresponding parameters were taken from Refs. [31,41]. The dominant interaction terms for dispersion forces come from dipole-dipole interactions, first derived by Drude [42]. We sum over all atoms in the lattice lying within a sphere of radius $R_{\max}$ large enough to guarantee convergence. For the three- and four-body force we chose $R_{\max} = 60$ Å, leading to converged results to the necessary precision used in this work.

Monte Carlo simulations. As discussed above, the melting temperature can be determined from two different approaches: either by direct determination of the T_m of the bulk, or from finite clusters where the melting temperature is obtained from extrapolation to the bulk. Similar to our previous work on rare gases [8,28,29,36], we adapt a Monte Carlo scheme to obtain the inner energy as a function of temperature. The temperature at which the solid-liquid phase transition occurs can be identified from a sudden increase in the inner energy, which corresponds to the temperature where the heat capacity curve $C(T)$ has a peak. The heat capacities $C_v(T)$ and $C_p(T)$, for the cluster and periodic simulations, respectively, are obtained from the relations

$$C_v(T) = \left.\frac{\partial U(T)}{\partial T}\right|_V = \frac{\langle U(T)^2\rangle - \langle U(T)\rangle^2}{k_BT^2}, \tag{4}$$

$$C_p(T) = \left.\frac{\partial H(T)}{\partial T}\right|_P = \frac{\langle H(T)^2\rangle - \langle H(T)\rangle^2}{k_BT^2}, \tag{5}$$

where the enthalpy is given by $H(T) = U(T) + PV$. With E_i being the total energy of a system of microstate i, the internal energy U is defined as the statistical mean value of energies E_i, $U = \langle E\rangle$.

For each simulated temperature 3×10^6 MC cycles are performed and statistical data are collected from the last 1×10^6 cycles. In total, 32 temperature trajectories are propagated simultaneously spanning the temperature interval of the melting transition. Exchanges of configurations are attempted of near-lying temperatures according to the parallel tempering method in order to overcome ergodicity problems and improve convergence. The temperature trajectories are connected through the parallel tempering method [7]; that is, an exchange is attempted between two neighboring temperature configurations with a 10% probability and an acceptance criteria based on the Boltzmann distribution. The statistical quantities such as the inner energy $U(T)$ and the heat capacity at constant volume, $C_v(T)$ (for finite cluster simulations), and volume $V(T)$, the enthalpy $H(T)$, and the heat capacity at constant pressure, $C_p(T)$ (for periodic simulations), are calculated using the two-body ELJ and three-body EATM potentials. These quantities are finally obtained as a continuous function of temperature T from the simulation data using the histogram reweighting technique [43]. In the following, specific details for the periodic and cluster simulations are given.

Periodic approach. Melting of the bulk is simulated using fcc sample cells with periodic boundary conditions. The simulations are performed in the isobaric-isothermal ensemble (NPT); that is, the number of atoms, N, and temperature T are held constant, but the sample cells are allowed to change volume V in order to remain at atmospheric pressure ($P =$ 1 bar) throughout the simulation. During the periodic constant pressure MC cycle $N + 1$ configurations are generated, where N is the number of atoms in the system. The test configuration is generated by either randomly selecting atom i and changing its coordinates from $\mathbf{r}_i \mapsto \mathbf{r}_i + \boldsymbol{\delta}_i$, or by varying the volume V with a randomly determined scaling parameter ς. The latter corresponds to the scaling of the volume V with ς^3, such that the new configuration is scaled as $\mathbf{r}_i \mapsto \varsigma\mathbf{r}_i$ and the length of the simulation cell by $L \mapsto \varsigma L$. In the NPT ensemble the probability density $\mathcal{P}$ to find a particular configuration of

N atoms at a given volume V is proportional to

$$\mathcal{P}(V;\mathbf{r}_i) \propto \exp(-\beta[E_i + PV - N\beta^{-1}\ln V]) \tag{6}$$

such that the acceptance criterion for either moving an atom or scaling the volume is given by

$$\alpha(x \to x') = \min[1, e^{-\beta[\Delta E + P\Delta V] + N\ln(V/V')}]. \tag{7}$$

Simulations are performed for fcc cells containing $N = (2k)^3 = 32$, 108, 256, 500, and 864 atoms considering two-body ELJ forces.

The total two-body interaction energy $E^{(2)}$ is determined by summing over all pairwise interactions up to a spherical cutoff distance of $r_c = \frac{1}{2}L$, where L is the length of the simulation cell. This method, known as the minimum image convention, approximates dispersive interaction between atom i and all periodic images of atom j by considering only interactions of an atom i with the closest image of atom j. The cutoff is introduced to avoid extensive mathematical calculations and potential energy jumps when one atom involved in the interaction moves out of the central box [44].

The total two-body energy in a system of density ρ with radial distribution function $g(r)$ can be split into a sum over the region $\{0, r_c\}$ and an integral over the long range $\{r_c, \infty\}$:

$$\begin{aligned} E^{(2)} &= E^{(2)}_{\mathrm{MC}} + E^{(2)}_{\mathrm{LRC}} \\ &= \sum_{i=1}^{N} E(r_{r_{ij}}) + 2\pi N\rho \int_{r_c}^{\infty} r^2 E\left(r_{r_{ij}}\right) g(r)\, dr \end{aligned} \tag{8}$$

Where $E^{(2)}_{\mathrm{MC}}$ is obtained during the MC simulation and the second part of the energy contribution is the long-range correction (LRC). The integral over the long range is numerically evaluated using Gauss-Legendre quadrature [45]. The radial distribution function $g(r)$ is approximated to be

$$g(r) = \exp[-\beta E^{(2)}(r)] \approx 1. \tag{9}$$

It is sufficient to calculate the integral in the tail correction only once at the beginning of the simulation, since the cutoff radius is held constant.

Additional simulations are performed considering two-body ELJ plus three-body EATM interactions for cells containing up to 256 atoms, with three-body contributions calculated up to a cutoff of $r = 2\sigma$ and for an $N = 32$ subcell as described by Attard [46], where σ is the position of the maximum of the three-body EATM potential.

The absence of a surface and impurities in the periodic melting simulations causes the simulated cells to shift the solid-to-liquid phase-transition temperature to a higher value due to superheating, $T_{\mathrm{SL}} > T_m$. We adapt the superheating correction factor as introduced by Belonoshko *et al.* [47] to obtain the bulk melting temperature T_m,

$$\frac{T_{\mathrm{SL}}}{T_m} = 1 + \frac{\ln 2}{3} \approx 1.231, \tag{10}$$

which worked well in previous simulations [28,29].

Cluster approach. For the rare gas elements the melting temperature decreases with an inverse dependence on the cluster radius [8,28], albeit for other elements such as metals a nonmonotonic behavior can be found at small to medium cluster sizes [48,49]. In the thermodynamic scaling range, however [49], it is possible to derive a relation between the melting temperature of a "spherical" cluster of N atoms, $T_m(N)$, and the corresponding bulk melting temperature, $T_m(\infty)$ [50]. One can obtain the relation starting from a first-order Taylor expansion of the chemical potential around its value at the triple point:

$$\mu(P,T) = \mu(P_0,T_0) + \frac{\partial\mu}{\partial T}(T - T_0) + \frac{\partial\mu}{\partial P}(P - P_0). \tag{11}$$

Since the chemical potentials for the solid and liquid phases are equal at the triple point, $\mu_s(P_0,T_0) = \mu_l(P_0,T_0)$, and using the Gibbs-Duhem equation, $-VdP + SdT + Nd\mu = 0$, we find

$$-S_l(T - T_0) + \frac{1}{\rho_l}(P_l - P_0) = -S_s(T - T_0) + \frac{1}{\rho_s}(P_s - P_0) \tag{12}$$

with $\rho = N/V$ being the cluster density. The Young-Laplace equation defines the pressure difference between the inside and the outside of a curved surface [51], which allows us to distinguish between the pressure $P_s = P_{\mathrm{ext}} + \frac{2\gamma_{sv}}{r_s}$ of a solid cluster and the pressure $P_l = P_{\mathrm{ext}} + \frac{2\gamma_{lv}}{r_l}$ of a liquid cluster, where γ_{sv} and γ_{lv} denote the solid-vapor and the liquid-vapor surface tensions, respectively. In both expressions the external pressure, P_{ext}, vanishes since clusters are being modeled in a vacuum. This, in combination with the latent heat of fusion, $L = (S_l - S_s)T_0$, the approximation that the triple point is approximately the melting temperature at ambient conditions, $T_0 \approx T_m(\infty)$, and the geometrical relationship which holds if

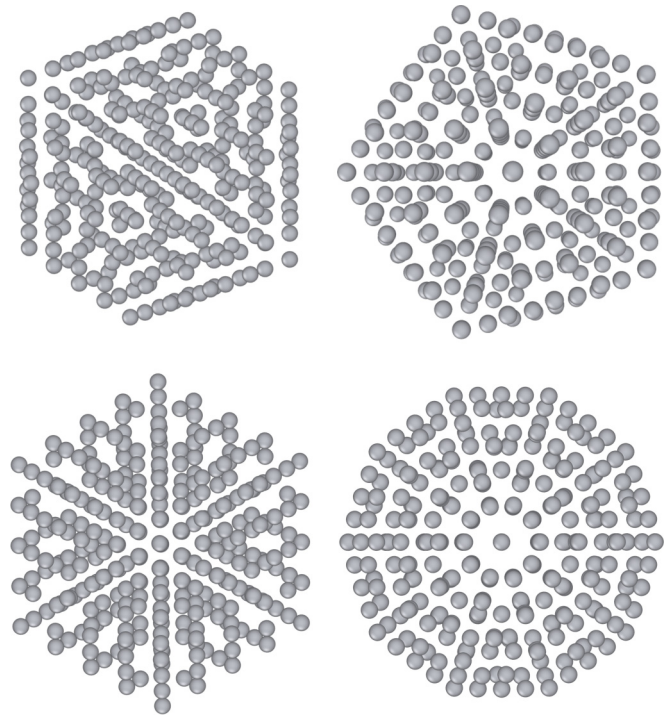

FIG. 1. Different orientations of the Mackay icosahedral cluster containing 309 atoms.

TABLE II. Solid-state properties for the fcc lattice of ^{84}Kr and ^{132}Xe at different levels of theory. The many-body expansion includes up to fourth-order terms in the interaction energy with individual contributions denoted as $E^{(n)}$. The nearest-neighbor distance r_{nn} is given in Å, volume V in cm^3/mol, cohesive energy E_{coh} in cm^{-1}, and bulk modulus B in GPa. EZPE-H denotes zero-point harmonic vibrational correction within the harmonic Einstein approximation for the two-body term only, EZPV-AH is the corresponding anharmonic correction from first-order perturbation theory. The fcc lattice constant a can be obtained from the nearest-neighbor distance through $a = \sqrt{2}r_{nn}$. ELJ, extended Lennard-Jones; JHBV, Jaeger-Hellmann-Bich-Vogel [35]; DS, Deiters-Sadus [58]; HJB, Hellmann-Jaeger-Bich [59]. All three-body forces are of extended Axilrod-Teller-Muto type from this work, and all four-body forces are obtained from the classical quadruple dipole term. For the diatomic molecules Kr_2 and Xe_2 we show for comparison the equilibrium distance r_e (in Å) and well depth D_e (in cm^{-1}; not corrected for zero-point vibration).

Property	Approx.	Kr (ELJ)	Kr (JHBV)	Kr (DS)	Xe (ELJ)	Xe (HJB)	Xe (DS)
r_e	$E^{(2)}$	4.0156	4.0158	4.0123	4.3616	4.3780	4.3748
	Expt.	4.008[a]				4.363,[a] 4.361,[b] 4.377(5)[c]	
r_{nn}	$E^{(2)}$	3.9345	3.9347	3.9315	4.2782	4.2911	4.2882
	+EZPV-H	3.9584	3.9586	3.9555	4.2941	4.3071	4.3043
	+EZPV-AH	3.9583	3.9584	3.9553	4.2940	4.3070	4.3042
	$+E^{(3)}$	4.0199	4.0199	4.0168	4.3296	4.3428	4.3399
	$+E^{(4)}$	4.0190	4.0192	4.0161	4.3283	4.3414	4.3385
	Expt.	3.9922(1)[d]			4.3358(3)[e]		
V	$E^{(2)}$	25.936	25.940	25.877	33.345	33.647	33.580
	+EZPV-H	26.412	26.416	26.353	33.717	34.025	33.958
	+EZPV-AH	26.409	26.412	26.350	33.716	34.021	33.955
	$+E^{(3)}$	27.663	27.662	27.597	34.560	34.878	34.808
	$+E^{(4)}$	27.645	27.647	27.582	34.530	34.844	34.773
	Expt.	27.095(3)[d]			34.708(8)[e]		
D_e	$E^{(2)}$	139.6	139.6	139.8	196.3	194.6	194.7
	Expt.	139.8, 140.2(5)			195.5(3.0),[b] 196.1(1.1)[c]		
E_{coh}	$E^{(2)}$	1076.3	1076.0	1078.6	1502.3	1489.3	1491.7
	+EZPV-H	1019.1	1019.0	1021.1	1451.6	1439.7	1441.8
	+EZPV-AH	1018.6	1018.5	1020.6	1451.4	1439.4	1441.5
	$+E^{(3)}$	916.1	916.0	917.2	1359.6	1350.5	1352.0
	$+E^{(4)}$	918.2	917.1	918.4	1362.6	1353.4	1354.9
	Expt.	931.9(10),[f] 934.6(14)[f]			1319.4(29),[f] 1326.1(23)[f]		
B	$E^{(2)}$	4.25	4.25	4.31	4.74	4.52	4.58
	+EZPV-H	3.89	3.89	3.94	4.48	4.28	4.33
	+EZPV-AH	3.89	3.89	3.94	4.48	4.28	4.33
	$+E^{(3)}$	3.50	3.50	3.55	4.21	4.01	4.05
	$+E^{(4)}$	3.55	3.54	3.59	4.15	3.98	4.06
	Expt.	3.61(5)[g]			3.64(8)[h]		

[a]Reference [60].
[b]Reference [61].
[c]Reference [62].
[d]Reference [63].
[e]References [64,65].
[f]Reference [66].
[g]Reference [67].
[h]Reference [68].

the particles have spherical shape $\frac{r_s}{r_l} = (\frac{\rho_l}{\rho_s})^{1/3}$ leads to the equation that describes the melting point depression:

$$1 - \frac{T_m(N)}{T_m(\infty)} = \frac{2}{\rho_s r_s L}\left(\gamma_{sv} - \gamma_{lv}\left(\frac{\rho_s}{\rho_l}\right)^{2/3}\right). \quad (13)$$

For our simulations, Mackay icosahedral clusters are chosen as initial structures for the solid state which are characterized by k complete shells of atoms around a central atom (see Fig. 1). The sizes of these so-called magic clusters with high stability are given by

$$N = 1 + 2\sum_{l=1}^{k}(5l^2 + 1) \quad (14)$$

$$= \frac{10}{3}k^3 + 5k^2 + \frac{11}{3}k + 1. \quad (15)$$

For large clusters, the dominating term of Eq. (14) is k^3, where k is the number of shells in the cluster. Since the radius r_s of an icosahedral cluster is proportional to the number of shells, k, $r_s \propto N^{-1/3}$. As ρ_s and ρ_l are constant, the melting temperature

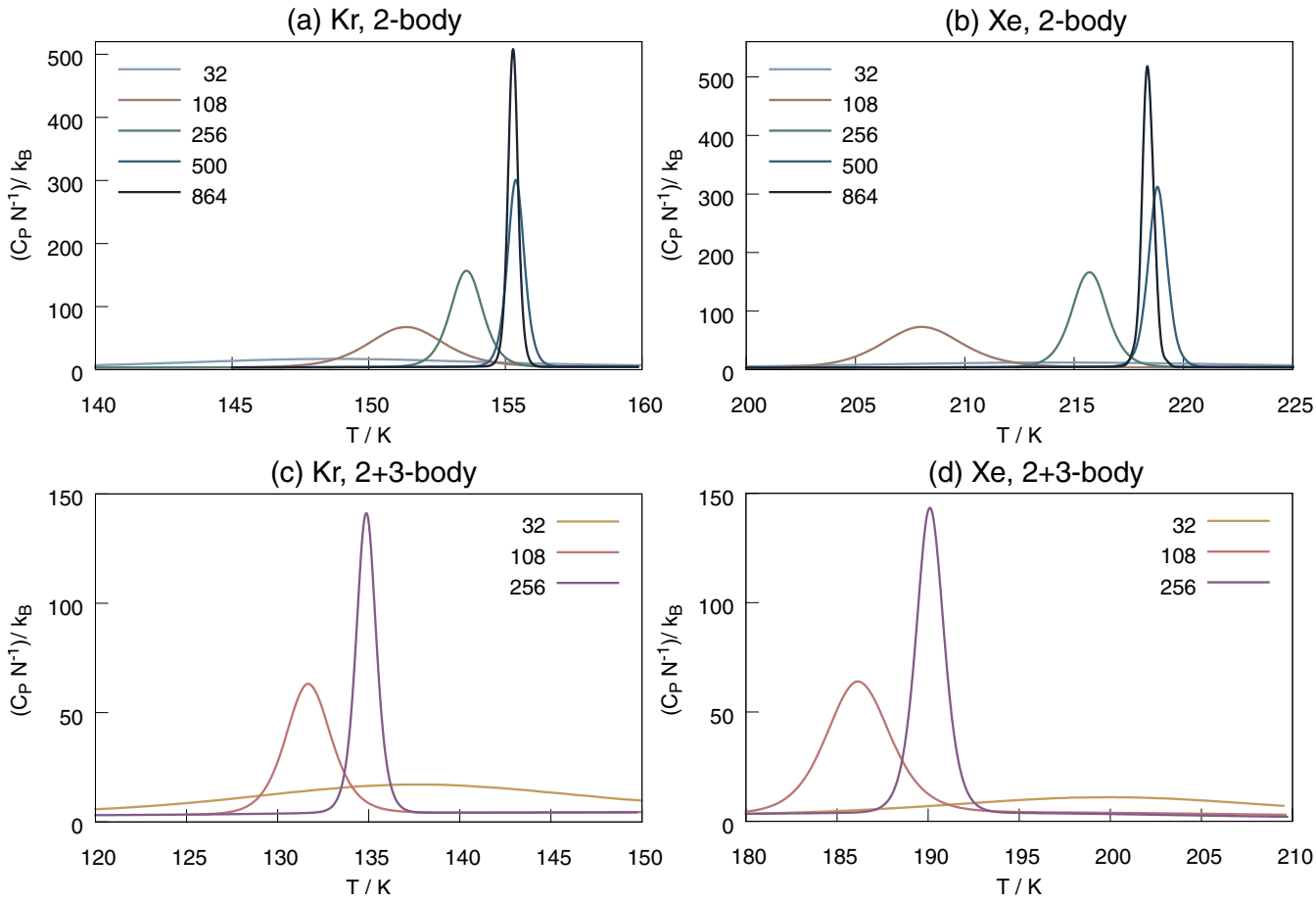

FIG. 2. Heat capacities at constant pressure as a function of simulated temperature per atom for the simulations with periodic boundary conditions: (a, b) heat capacities obtained considering two-body ELJ interactions only and (c, d) heat capacities obtained considering both two- and three-body interactions (ELJ+EATM).

of a cluster with N atoms is related to the melting temperature by

$$T_m(N) = T_m(\infty)\left(1 - \frac{\mathcal{C}}{N^{1/3}}\right). \tag{16}$$

This implies that it is possible to linearly extrapolate the melting temperatures of the different cluster sizes to the bulk melting temperature with the inverse cluster radius $N^{-1/3}$. Smaller clusters ($k = 1, 2$) are expected to deviate from this line since the k^3 term is smaller than the terms with lower order in k in Eq. (16) and the error in the obtained bulk value is expected to reduce when clusters of larger size N are included in the extrapolation.

Over the years multiple efforts have been made to express a more accurate equation describing the melting point depression. A review of these models can be found in Ref. [52]. One improvement can be made by including the possibility of surface melting, first developed by Reiss and Wilson [53] and later developed by Hanszen [54], Sambles [55], and Chushak and Bartell [56]. In this scheme, the clusters are assumed to have an inner core and an external liquid shell of thickness δ. The liquid layer over the solid core remains unchanged until the particle cluster transforms completely to a liquid at the melting temperature. However, these more accurate relations are described by more complex functions with more fitting parameters which give rise to large uncertainties in the extrapolated temperature when only few data points are considered.

Melting simulations were performed for Mackay icosahedral clusters of size $N = 13, 55, 147, 309, 561, 923$, and 1415 atoms considering two-body interactions only; additional simulations were performed considering two- and three-body interactions up to clusters containing 923 atoms. To keep the clusters from evaporating, a hard sphere is defined with a radius of one diatomic equilibrium distance larger than the radius of the icosahedral cluster. For this type of simulation the hard-sphere volume V is thus held constant during the MC simulation and the acceptance criterion simplifies to

$$\alpha(x \to x') = \min[1, e^{-\beta \Delta E}]. \tag{17}$$

Two-body interactions are considered over the entire sphere, whereas for the three-body interaction a cutoff radius of $r = 2\sigma$ is employed, where σ is the position of the maximum of the three-body EATM potential. Of course, one is not confined to simulations of magic-number clusters only and the same simulating procedure can be applied to other particle sizes and configurations [57]. However, due to their closed-shell structure, surface effects are minimized with respect to the clusters with incomplete shells.

III. RESULTS AND DISCUSSION

Solid-state calculations. The results for the dimer equilibrium distances and bulk properties are presented in Table II in comparison with experimental results (citations as specified in the table's caption) and with results obtained from other accurate diatomic potential curves, namely those of Jäger, Hellmann, and co-workers (JHBV) [35,59], and Deiters and Sadus (DS) [58]. We see very good agreement for the bond distances and the dissociation energies with the other theoretical results and with available experimental data.

Concerning the solid-state results, we see that the destabilizing three-body forces cannot be neglected anymore; i.e., they account for −11.2% and −17.4% of the total cohesive energy for Kr and Xe, respectively. In comparison, vibrational effects (−6.3% for Kr and −3.7% for Xe) and four-body forces (+0.2% for both Kr and Xe) contribute much less to the cohesive energy. Considering all terms we get a bond distance which is 0.027 Å above and 0.008 Å below the experimental values for Kr and Xe, respectively, which is most likely due to the approximations made for the three-body force. The discrepancies are somewhat larger for the cohesive energies with a deviation of 13 and 37 cm^{-1} for Kr and Xe, respectively. However, these values are in the acceptable range of the reported experimental uncertainties, and the three-body contributions are of similar size as those reported by Rościszewski *et al.* [33]. We notice, however, the different sign and order of magnitude of the four-body contribution by these authors [33]. The bulk moduli are also in reasonable agreement with experiment. In conclusion, for the melting simulations discussed below it is sufficient to include only two- and three-body forces.

Melting temperatures. The heat capacity curves from the periodic boundary simulations of Kr and Xe are shown in Fig. 2, where the heat capacities at constant pressure are plotted against the simulation temperature. The corresponding melting temperatures, corrected by the superheating correction factor, Eq. (10), are listed in Table III, and the total two- and three-body energy contribution for an equilibrated liquid cell as a function of the cut-off radius is demonstrated in Fig. 3.

One can immediately observe a correlation between the melting temperature and the total dispersive interaction for different cell sizes. However, note that the energy contribution does not necessarily exactly scale with melting temperature, as the contribution beyond the cutoff distance is approximated by the tail correction. For the smallest cell considered, containing only 32 atoms, the total energy contribution is not converged which is manifested in a depression in the melting point, a reduction in the latent heat of melting, and a finite broadening ΔT_m around the melting point [69]. All of the above-mentioned finite-size effects decrease with increasing cell size. For the largest cell considered, the energy contribution is converged, and the finite-size effects are minimal.

TABLE III. Melting temperatures (in K) extracted from the heat capacity curves obtained by periodic *NPT* melting simulations and corrected by the superheating factor introduced in Eq. (10) for the employed N atomic cells.

		$N = 32$	108	256	500	864
Krypton	Two-body	120.81	122.96	124.76	126.22	126.15
	Two- and three-body	111.82	106.96	109.56		
	Δ_{3b}	8.99	15.99	15.21		
Xenon	Two-body	173.98	168.98	175.22	177.74	176.84
	Two- and three-body	162.33	151.22	154.44		
	Δ_{3b}	11.65	17.76	20.78		

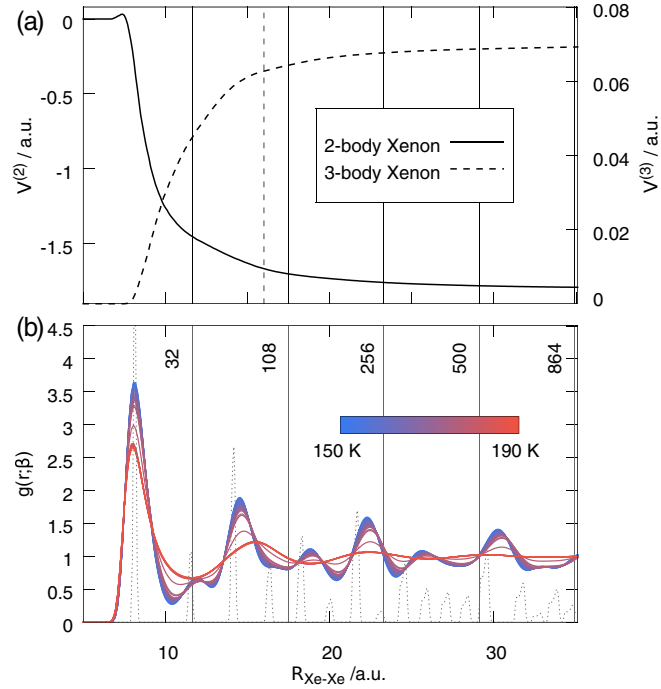

FIG. 3. (a) The total two- (solid line) and three-body (dotted line) contribution as a function of the cutoff radius. The vertical lines denote the spherical two-body cutoff radius that is implemented for the different simulated sizes such that the minimum image convention is satisfied. The vertical dashed line corresponds to the three-body cutoff radius, which is held fixed for the different sample sizes. (b) Pair distribution function $g(r, \beta)$ of xenon between 150 and 190 K for a simulation with periodic boundary conditions. Near T_m the fcc lattice breaks down to form a disordered fluid. The gray dotted line indicates a near-perfect initial fcc structure.

For both simulated elements, the $N = 864$ cell has a very small difference in melting temperature compared to the $N = 500$ cell and even lies slightly below the melting temperature of the $N = 500$ cell. It is therefore concluded that for the $N = 864$ cell the melting temperature has converged and lies within the range of statistical error.

The three-body corrections are estimated from the difference in melting temperature between the two-body and the two- and three-body calculation at size $N = 256$. The largest contribution to the error is expected to evolve from this approximation since tail corrections are not considered for the three-body contributions. Besides, the three-body correction is determined from a rather small cell with only three-body contributions considered up to $r_{co} = 2\sigma$.

Turning to the cluster simulations, Fig. 4 shows the heat capacities for Kr_N and Xe_N. While these curves are unimodal

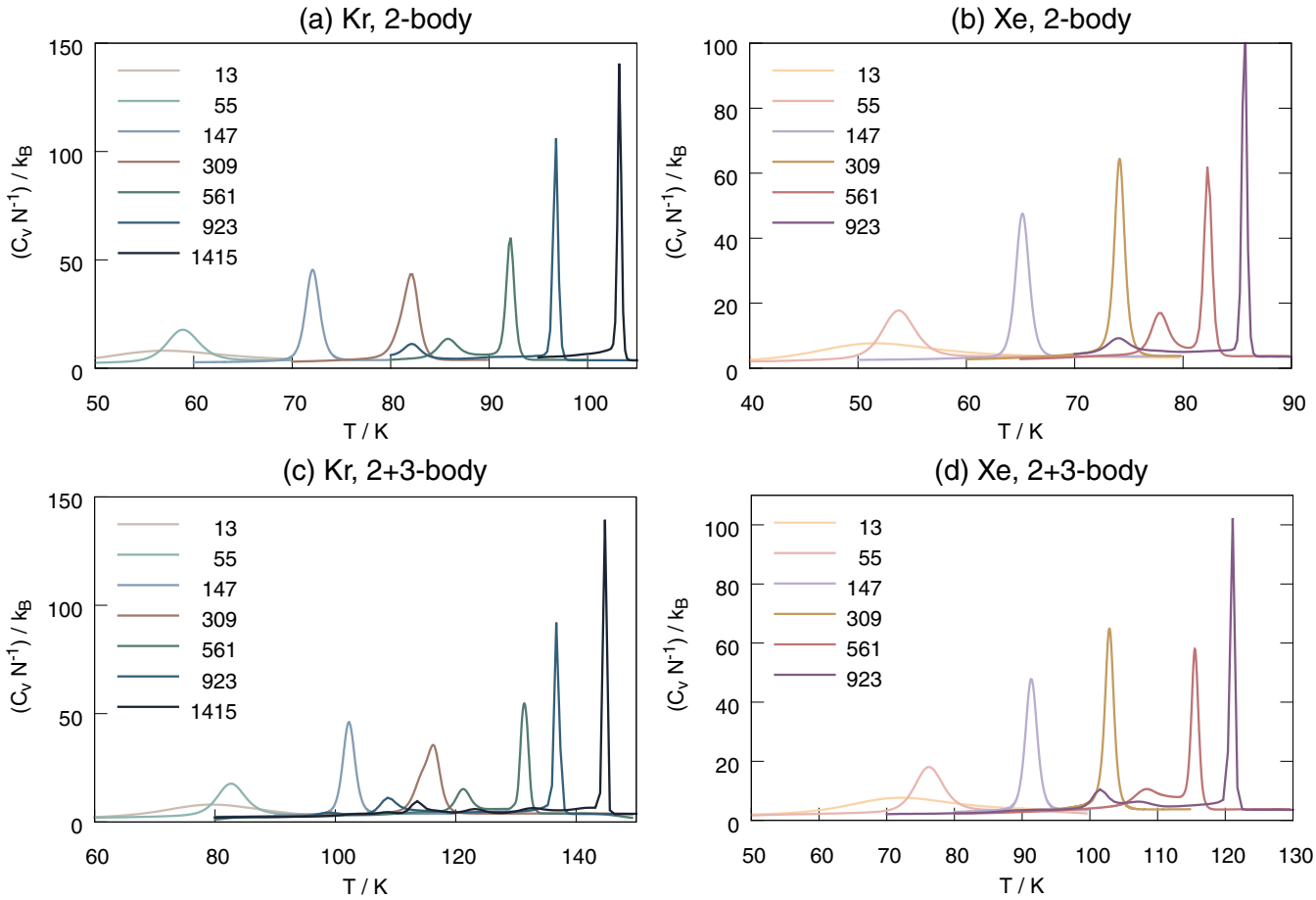

FIG. 4. Heat capacities at constant volume as a function of temperature per atom for the Mackay icosahedral clusters with up to 1415 atoms for krypton and xenon: (a, b) heat capacity curves obtained considering two-body interactions only, using the ELJ potential, and (c, d) heat capacities obtained considering two- and three-body interactions, computed with the ELJ and EATM potentials, respectively.

up to clusters containing 147 atoms, additional peaks are also present in the larger simulated clusters. These additional peaks are associated with surface reconstruction (premelting) [8,70]. The melting temperatures are determined from the equilibrium heat capacity as the maximum of the heat capacity curves and are listed in Table IV. By plotting the melting temperatures as a function of $N^{-1/3}$, as shown in Fig. 5, the melting temperatures exhibit a linear trend at larger N values and can be extrapolated to the bulk value. The two smallest clusters of size $N = 13$ and $N = 55$ deviate from this line as to be expected [see the discussion below Eq. (16)] and are therefore not considered in the extrapolation. The extrapolated melting temperatures are listed in Table V, where the two-body melting temperature is obtained by extrapolation for cluster sizes $N = 147-1415$. It is computationally too expensive to obtain the three-body corrected melting temperature of the 1415 cluster. Therefore, three-body corrections are taken as the difference in melting temperature when extrapolating clusters of size $N = 147$–923 including two- and three-body interactions and including two-body interaction only. This difference gives the extrapolated three-body correction which is then added to the extrapolated two-body melting temperature from the 147–1415 extrapolation.

For krypton, two-body melting temperatures are calculated to be $T^{p}_{m,2b} = 126.2$ and $T^{c}_{m,2b} = 129.7$ K for the periodic (p) and cluster (c) simulations, respectively (see Table VI). The

TABLE IV. Melting temperatures (in K) for the krypton and xenon rare gas clusters extracted from the heat capacity curves.

	N=13	55	147	309	561	923	1415
			Krypton				
Two-body	57.12	58.90	72.07	82.10	92.15	96.80	103.20
Two- and three-body	51.63	53.75	65.18	74.15	82.27	85.72	
			Xenon				
Two-body	79.56	82.66	102.26	115.56	129.85	136.50	144.80
Two- and three-body	72.07	76.22	91.36	102.89	115.50	121.10	

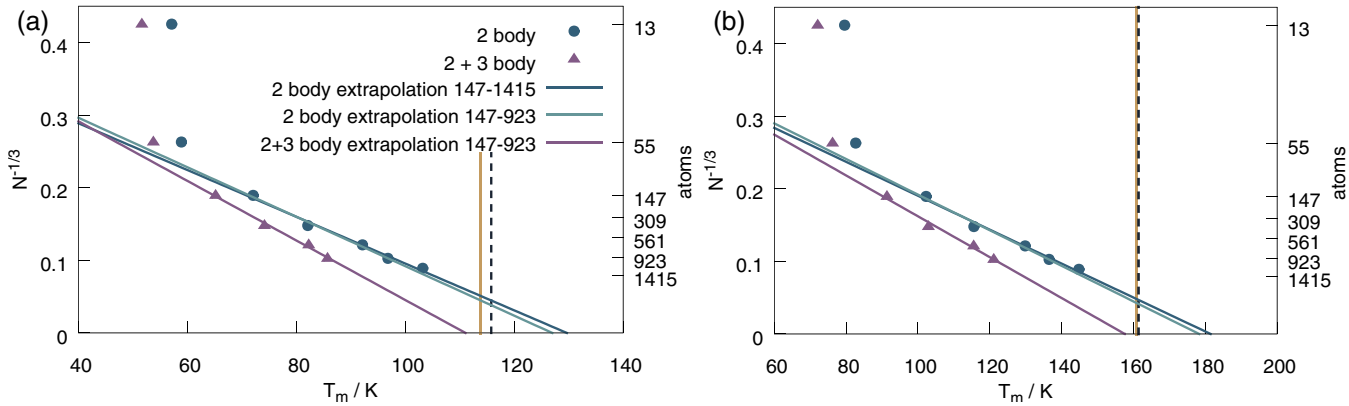

FIG. 5. Extrapolated melting temperatures for (a) krypton and (b) xenon, obtained using two-body ELJ interactions (circles) and three-body-corrected EATM values (triangles). The blue line corresponds to the linear fit of the melting temperatures of the $N = 147-1415$ ELJ clusters, light blue corresponds to the melting temperatures of the $N = 147$–923 ELJ clusters, and the purple line corresponds to the linear fit through the $N = 147-923$ clusters including three-body EATM corrections. The experimental melting points of the bulk are indicated as dotted vertical lines and our computed value by the solid orange vertical lines.

lowering in melting temperature due to the three-body repulsive forces is similar for both approaches ($T^p_{m,3b} = 15.2$ K and $T^c_{m,3b} = 15.9$ K, respectively). The final melting temperatures are determined to be $T^p_m = 110.9$ K and $T^c_m = 113.7$ K. These values of T_m are slightly lower than the experimental value of 115.78 K. For xenon the two-body melting temperatures are determined to be $T^p_{m,2b} = 176.8$ K and $T^c_{m,2b} = 181.5$ K. The lowering in melting temperature due to the three-body repulsion is for both methods fairly similar ($T^p_{m,3b} = -20.8$ and $T^c_{m,3b} = -20.7$ K). The final melting temperatures are determined to be $T^p_m = 156.1$ K and $T^c_m = 160.8$ K, of which the cluster result is in very good agreement with the experimental value of 161.40 K.

Densities. The density of frozen polycrystalline krypton was experimentally obtained by Figgins and Smith in 1960 [71] using x-ray diffractive methods (3.078 g/cm^3 at 20 K and 2.893 g/cm^3 at 90 K), using the same method to determine the thermodynamic properties for solidified argon [72]. Calado and Staveley [73] measured the liquid density of krypton close to the melting point and determined it to be 2.4517 g/cm^3 at 115.77 K. The latest experimental data were obtained in 1980 by Albuquerque *et al.* [74], who obtained a density of 2.3483 to 2.1983 g/cm^3 for the temperature range of $T = 129.32-147.08$ K. These values are in excellent agreement with the numerical results obtained from the periodic simulation shown in Fig. 6; before melting starts we obtain a density of solid krypton of 2.727 g/cm^3 (107 K), which slightly decreases to 2.316 g/cm^3 (111 K) for the liquid phase using a mass of 83.798 g/mol. For comparison, the solid density at 0 K obtained from the volume in Table II is much higher compared to the liquid state at 3.031 g/cm^3 (experimental value 3.093 g/cm^3) [63].

The densities for xenon at normal pressure are perhaps the most easy to obtain in comparison to the other noble gases as xenon is not radioactive and offers the widest accessible range of temperatures for the solid and liquid states at normal pressures. The first density measurements of solid xenon date back to Sears and Klug [64] and Eatwell and Smith [65], who carried out measurements in the 1960s on the expansivity and density of frozen polycrystalline xenon according to the same x-ray diffractive method as for argon and krypton. Densities of 3.694 g/cm^3 and 3.689 g/cm^3 at 60 K by Sears and Kulg and by Eatwell and Smith were obtained, respectively. The density of liquid xenon was determined by Leadbetter and Thomas [75] according to the bulk density method, where the density of a liquid is determined by condensing a known mass of gas into a volume-calibrated glass capillary tube. They obtained a liquid density of 2.980 g/cm^3 at 161.9 K. A summary of the liquid density of krypton and xenon around the melting point can be found in Ref. [76]. Regarding the MC results, the solid density (3.317 g/cm^3 at 152 K) is lower than the experimentally obtained values. However, this can be attributed to thermal expansion at that temperature compared to the 60 K value. Indeed, the density of the liquid (2.845 g/cm^3 at 157 K)

TABLE V. Melting temperatures (in K) obtained by linear extrapolation of $N^{-1/3}$ to the bulk melting temperature. Δ_{3b} denotes the difference between the two- and three-body result.

	N	Two-body	Two- + three-body	Δ_{3b}
Krypton	[147–1415]	129.66		
	[147–923]	126.99	111.05	15.94
	Δ	2.67		
Xenon	[147–1415]	181.47		
	[147–923]	178.29	157.60	20.69
	Δ	3.18		

TABLE VI. Periodic and cluster final melting temperatures (in K).

		Periodic	Cluster	Expt.
Krypton	2b	126.15	129.66	
	$\Delta_{(2b-3b)}$	15.21	15.94	
	T_m	110.94	113.72	115.78
Xenon	2b	176.84	181.47	
	$\Delta_{(2b-3b)}$	20.78	20.69	
	T_m	156.07	160.78	161.40

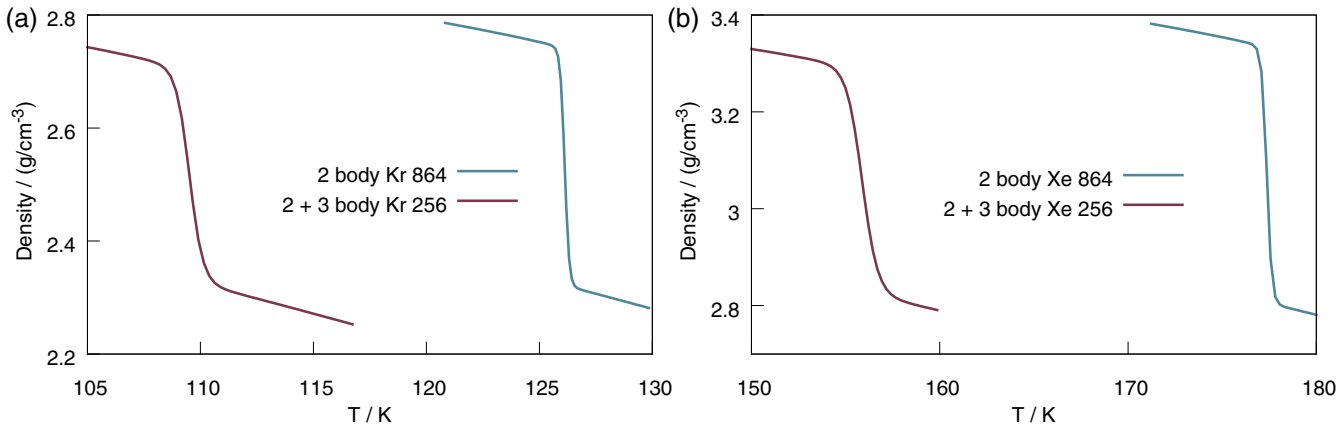

FIG. 6. Density curves for (a) krypton and (b) xenon. Blue denotes the densities for the MC simulations including two-body ELJ interactions only, and red denotes the densities obtained including two-body ELJ and three-body EATM interactions.

is in good agreement with experimental results. The solid density at 0 K obtained from the calculated volume in Table II is 3.802 g/cm^3 and much higher compared to the liquid state as one expects, and again in excellent agreement with the experimental value of 3.783 g/cm^3 (a mass of 131.293 g/mol for xenon is used for the calculations).

IV. CONCLUSIONS

We have calculated the melting temperatures of krypton and xenon using first-principles two- and three-body potentials. The obtained melting temperatures by direct simulation of the bulk (Kr = 110.94 K and Xe = 156.07 K) and by the cluster approach (Kr = 113.72 K and Xe = 160.78 K) are in excellent agreement with experimental findings. Concerning error estimates there are multiple sources for errors involved. They come from (i) the choice of the interaction potentials (e.g., the description of the three-body interactions needs to be improved), (ii) the algorithm for the melting simulation used, (iii) the extrapolation to the bulk temperature for finite clusters, (iv) for a cell with periodic boundary conditions the number of atoms used in the cell and the estimate of the superheating correction factor, and (v) the neglect of quantum and/or vibrational effects. The close correspondence between the cluster and periodic results, however, implies that we can confide in the Monte Carlo method. Even though in a previous paper by our group [8] an accuracy of the melting temperature within 1–2 K was achieved for neon and argon, it is in no way trivial to achieve similar accuracy for the heavier rare gases as large relativistic and correlation effects require higher-order terms in the many-body expansion. However, while the computational protocol can still be improved, our results differ at most by 5 K from experiment.

ACKNOWLEDGMENTS

We acknowledge financial support by the Alexander-von-Humboldt Foundation (Bonn) and the Marsden Fund (14-MAU-034) of the Royal Society of New Zealand (Wellington). We thank Dr. Jan Mewes for interesting and stimulating discussions.

[1] U. R. Pedersen, L. Costigliola, N. P. Bailey, T. B. Schrøder, and J. C. Dyre, Nat. Commun. **7**, 12386 (2016).
[2] F. A. Lindemann, Phys. Z. **11**, 609 (1910).
[3] R. Etters and J. Kaelberer, Phys. Rev. A **11**, 1068 (1975).
[4] R. Etters and J. Kaelberer, J. Chem. Phys. **66**, 5112 (1977).
[5] R. S. Berry, T. L. Beck, H. L. Davis, and J. Jellinek, Adv. Chem. Phys. **70B**, 75 (1988).
[6] L. Brillouin, Phys. Rev. **54**, 916 (1938).
[7] R. H. Swendsen and J.-S. Wang, Phys. Rev. Lett. **57**, 2607 (1986).
[8] E. Pahl, F. Calvo, L. Koči, and P. Schwerdtfeger, Angew. Chem. Int. Ed. **47**, 8207 (2008).
[9] P. Schwerdtfeger, N. Gaston, R. P. Krawczyk, R. Tonner, and G. E. Moyano, Phys. Rev. B **73**, 064112 (2006).
[10] F. Perakis, K. Amann-Winkel, F. Lehmkühler, M. Sprung, D. Mariedahl, J. A. Sellberg, H. Pathak, A. Späh, F. Cavalca, D. Schlesinger, A. Ricci, A. Jain, B. Massani, F. Aubree, C. J. Benmore, T. Loerting, G. Grübel, L. G. M. Pettersson, and A. Nilsson, Proc. Natl. Acad. Sci. USA **114**, 8193 (2017).
[11] S.-N. Luo, A. Strachan, and D. C. Swift, J. Chem. Phys. **120**, 11640 (2004).
[12] L. Zheng, S.-N. Luo, and D. L. Thompson, J. Chem. Phys. **124**, 154504 (2006).
[13] S. R. Phillpot, J. F. Lutsko, D. Wolf, and S. Yip, Phys. Rev. B **40**, 2831 (1989).
[14] J. Solca, A. J. Dyson, G. Steinebrunner, B. Kirchner, and H. Huber, J. Chem. Phys. **108**, 4107 (1998).
[15] G. F. Velardez, S. Alavi, and D. L. Thompson, J. Chem. Phys. **120**, 9151 (2004).
[16] F. J. Allen and R. Moore, J. Am. Chem. Soc. **53**, 2522 (1931).
[17] W. Keesom, J. Mazur, and J. Meihuizen, Physica **2**, 669 (1935).
[18] M. P. Freeman and G. Halsey, Jr., J. Chem. Phys. **60**, 1119 (1956).

[19] K. D. Hill, AIP Conf. Proc. **1552**, 198 (2013).
[20] W. Ramsay and M. W. Travers, Philos. Trans. R. Soc. London A **197**, 47 (1901).
[21] G. Kane, J. Chem. Phys. **7**, 603 (1939).
[22] W. M. Haynes, *CRC Handbook of Chemistry and Physics* (CRC Press, Boca Raton, FL, 2014).
[23] A. Ferreira and L. Q. Lobo, J. Chem. Thermodyn. **40**, 618 (2008).
[24] P. Schwerdtfeger, R. Tonner, G. E. Moyano, and E. Pahl, Angew. Chem. Int. Ed. **55**, 12200 (2016).
[25] K. K. Nanda, S. N. Sahu, and S. N. Behera, Phys. Rev. A **66**, 013208 (2002).
[26] K. G. Steenbergen, E. Pahl, and P. Schwerdtfeger, J. Phys. Chem. Lett. **8**, 1407 (2017).
[27] R. W. Gray and W. Ramsay, J. Chem. Soc. Trans. **95**, 1073 (1909).
[28] O. R. Smits, P. Jerabek, E. Pahl, and P. Schwerdtfeger, Angew. Chem. Int. Ed. **57**, 9961 (2018).
[29] J. Wiebke, E. Pahl, and P. Schwerdtfeger, Angew. Chem. Int. Ed. **52**, 13202 (2013).
[30] P. Jerabek, O. Smits, E. Pahl, and P. Schwerdtfeger, Mol. Phys. **116**, 1 (2018).
[31] P. Schwerdtfeger and J. K. Nagle, Mol. Phys. **117**, 1200 (2019).
[32] K. Rościszewski, B. Paulus, P. Fulde, and H. Stoll, Phys. Rev. B **60**, 7905 (1999).
[33] K. Rościszewski, B. Paulus, P. Fulde, and H. Stoll, Phys. Rev. B **62**, 5482 (2000).
[34] A. Hermann, R. P. Krawczyk, M. Lein, P. Schwerdtfeger, I. P. Hamilton, and J. J. P. Stewart, Phys. Rev. A **76**, 013202 (2007).
[35] B. Jäger, R. Hellmann, E. Bich, and E. Vogel, J. Chem. Phys. **144**, 114304 (2016).
[36] E. Pahl, F. Calvo, and P. Schwerdtfeger, Int. J. Quantum Chem. **109**, 1812 (2009).
[37] H.-J. Werner, P. J. Knowles, G. Knizia, F. R. Manby, M. Schütz, P. Celani, W. Györffy, D. Kats, T. Korona, R. Lindh, A. Mitrushenkov, G. Rauhut, K. R. Shamasundar, T. B. Adler, R. D. Amos, A. Bernhardsson, A. Berning, D. L. Cooper, M. J. O. Deegan, A. J. Dobbyn, F. Eckert, E. Goll, C. Hampel, A. Hesselmann, G. Hetzer, T. Hrenar, G. Jansen, C. Köppl, Y. Liu, A. W. Lloyd, R. A. Mata, A. J. May, S. J. McNicholas, W. Meyer, M. E. Mura, A. Nicklass, D. P. O'Neill, P. Palmieri, D. Peng, K. Pflüger, R. Pitzer, M. Reiher, T. Shiozaki, H. Stoll, A. J. Stone, R. Tarroni, T. Thorsteinsson, and M. Wang, MOLPRO, version 2015.1, A package of *ab initio* programs (2015).
[38] W. Cencek, G. Garberoglio, A. H. Harvey, M. O. McLinden, and K. Szalewicz, J. Phys. Chem. A **117**, 7542 (2013).
[39] P. Schwerdtfeger and A. Hermann, Phys. Rev. B **80**, 064106 (2009).
[40] W. Bade, J. Chem. Phys. **28**, 282 (1958).
[41] C. Johnson and T. Spurling, Aust. J. Chem. **27**, 241 (1974).
[42] P. Drude, *The Theory of Optics* (Longmans, Green and Co., New York, 1902).
[43] A. M. Ferrenberg and R. H. Swendsen, Phys. Rev. Lett. **61**, 2635 (1988).
[44] N. Metropolis, A. W. Rosenbluth, M. N. Rosenbluth, A. H. Teller, and E. Teller, J. Chem. Phys. **21**, 1087 (1953).
[45] M. P. Allen and D. J. Tildesley, *Computer Simulation of Liquids* (Oxford University Press, Oxford, UK, 2017).
[46] P. Attard, Phys. Rev. A **45**, 5649 (1992).
[47] A. B. Belonoshko, N. V. Skorodumova, A. Rosengren, and B. Johansson, Phys. Rev. B **73**, 012201 (2006).
[48] I. Hamid, M. Fang, and H. Duan, AIP Adv. **5**, 047129 (2015).
[49] A. Yalamanchali, K. L. Pyfer, and M. F. Jarrold, J. Phys. Chem. C **121**, 10242 (2017).
[50] P. Pawlow, Z. Phys. Chem. **65**, 545 (1909).
[51] R. Defay and I. Prigogine, *Surface Tension and Adsorption* (Wiley, New York, 1966).
[52] F. Baletto and R. Ferrando, Rev. Mod. Phys. **77**, 371 (2005).
[53] H. Reiss and I. B. Wilson, J. Colloid Sci. **3**, 551 (1948).
[54] K.-J. Hanszen, Z. Phys. **157**, 523 (1960).
[55] J. R. Sambles, Proc. R. Soc. A **324**, 339 (1971).
[56] Y. G. Chushak and L. S. Bartell, J. Phys. Chem. B **105**, 11605 (2001).
[57] F. Senn, J. Wiebke, O. Schumann, S. Gohr, P. Schwerdtfeger, and E. Pahl, J. Chem. Phys. **140**, 044325 (2014).
[58] U. K. Deiters and R. J. Sadus, J. Chem. Phys. **150**, 134504 (2019).
[59] R. Hellmann, B. Jäger, and E. Bich, J. Chem. Phys. **147**, 034304 (2017).
[60] J. Ogilvie and F. Y. Wang, J. Mol. Struct. **273**, 277 (1992).
[61] D. E. Freeman, K. Yoshino, and Y. Tanaka, J. Chem. Phys. **61**, 4880 (1974).
[62] A. Wüest, U. Hollenstein, K. G. de Bruin, and F. Merkt, Can. J. Chem. **82**, 750 (2004).
[63] D. L. Losee and R. O. Simmons, Phys. Rev. **172**, 944 (1968).
[64] D. R. Sears and H. P. Klug, J. Chem. Phys. **37**, 3002 (1962).
[65] A. Eatwell and B. Smith, Philos. Mag. **6**, 461 (1961).
[66] L. A. Schwalbe, R. K. Crawford, H. H. Chen, and R. A. Aziz, J. Chem. Phys. **66**, 4493 (1977).
[67] J. Skalyo, Y. Endoh, and G. Shirane, Phys. Rev. B **9**, 1797 (1974).
[68] N. A. Lurie, G. Shirane, and J. Skalyo, Phys. Rev. B **9**, 2661 (1974).
[69] F. Calvo, Front. of Nanosci. **12**, 295 (2018).
[70] C. Hock, C. Bartels, S. Straßburg, M. Schmidt, H. Haberland, B. von Issendorff, and A. Aguado, Phys. Rev. Lett. **102**, 043401 (2009).
[71] B. F. Figgins and B. L. Smith, Philos. Mag. **5**, 186 (1960).
[72] E. R. Dobbs and G. O. Jones, Rep. Prog. Phys. **20**, 516 (1957).
[73] J. C. G. Calado and L. A. K. Staveley, Fluid Phase Equilib. **3**, 153 (1979).
[74] G. Albuquerque, M. N. Da Ponte, and L. Staveley, Cryogenics **20**, 416 (1980).
[75] A. J. Leadbetter and H. E. Thomas, Trans. Faraday Soc. **61**, 10 (1965).
[76] A. G. Ferreira and L. Q. Lobo, J. Chem. Thermodyn. **41**, 809 (2009).